Microphone-Array Measurements on a Scaled Model in ETW at Real-Flight Reynolds Numbers

Thomas Ahlefeldt *

Institute of Aerodynamics and Flow Technology

German Aerospace Center, D-37073 Göttingen, Germany

This paper presents an experimental investigation of small-scale model airframe noise at various Reynolds numbers up to the real-flight case. The study consists of data acquired with a microphone array in the European Transonic Windtunnel (ETW). The advantage of the ETW is to enable testing simultaneously at cryogenic temperatures and increased pressure levels, which extends the range of achievable Reynolds numbers up to those pertaining to full-scale flight conditions. At the German Aerospace Center (DLR), the microphone-array measurement technique has been further developed to perform measurements under combined cryogenic and pressurized conditions. For this purpose, a microphone-array consisting of 96 microphones was designed and constructed. In this paper, aeroacoustic results are presented for various Reynolds numbers up to the real-flight case on an Airbus K3DY half-model of scale 1:13.6. The results showed significant Reynolds number and Mach number dependency for various sources. Of particular note are various dominant sources appearing on the flap at real-flight Reynolds numbers. To the authors knowledge, this is the first time that airframe noise data for a small-scale model have been acquired at real-flight Reynolds numbers.

Nomenclature

*Research Associate, German Aerospace Center. Associated member AIAA.

α	angle-of-attack	p_{stat}	static pressure
δ	mean aerodynamic chord length	p'	acoustic pressure fluctuations
γ	adiabatic index	$\hat{\mathbf{R}}$	spectral cross-correlation matrix
ω	angular frequency	$\hat{\mathbf{R}}_{DR}$	$\hat{\mathbf{R}}$ with diagonal term set to zero
ρ	density	$\mathcal{R}$	molar gas constant
ρ'	acoustic density fluctuations	q	dynamic pressure
a	speed of sound	r	distance source to observer
D	length scale	r_0	reference distance
E	Young's modulus	Re_δ	Reynolds number based on δ
$\mathbf{e}$	steering vector	St_δ	Strouhal number based on δ
f	frequency	$\hat{S}$	delay-and-sum array output
f_{fs}	full scale frequency	SD	standard deviation
$\mathcal{H}$	conjugate transpose	T	temperature
I	acoustic intensity	u_∞	free stream velocity
L_p	Sound pressure level	x, y, z	spatial coordinates
m_{mol}	molar mass	$\mathbf{y}_f$	focus point vector
M	Mach number		
N	number of microphones		

I.   Introduction

The use of phased microphone arrays to acquire acoustic data of scaled models in standard wind tunnels with a closed test section has become a standard measurement technique. As shown by Stoker[1], results obtained in a standard wind tunnel show differences when compared with results obtained from real flight tests: these differences can be attributed to lack of model-fidelity, installation effects, a discrepancy in Reynolds number, and to the applicability of the assumptions made in phased array processing. The present paper will address the effect of the Reynolds number in such measurements.

Aerodynamic measurements are often performed in cryogenic and/or pressurized wind tunnels which are capable of achieving real-flight Reynolds number flows; conventional wind tunnels cannot generally achieve real-flight Reynolds numbers. Aeroacoustic measurements, however, have so far not been performed at real-flight Reynolds numbers on a small-scale aircraft model (i.e. under combined cryogenic and pressurized conditions).

Promising studies have been carried out in the past under different conditions. Hayes[2] performed measurements under pressurized conditions up to 466 kPa, where the results indicated that aeroacoustic source mechanisms depend on the Reynolds number, especially at high frequencies. However, as remarked by Stoker et al.,[3] even pressurized wind tunnels can-

not generally achieve real-flight Reynolds numbers. Consequently, Stoker successfully carried out measurements in a combined mildly cryogenic and pressurized environment at temperatures down to 226.5 K as a proof-of-concept study. But to achieve real-flight Reynolds numbers (the increase in Reynolds number is especially pronounced at lower temperatures), measurements have to be carried out in a fully cryogenic environment down to temperatures below 120 K.

In a first step, as previously presented by the author[4,5], the microphone array measurement technique for cryogenic application down to 100 K has been developed and successfully applied to a high-lift configuration. Those measurements took place at the DNW cryogenic wind tunnel located at the DLR Cologne site (Kryo-Kanal Koeln, DNW-KKK).

For the next step, this paper will focus on acquiring aeroacoustic data in an environment which is both pressurized and fully cryogenic. The facility of the European Transonic Wind-tunnel GmbH (ETW) can provide real-flight Reynolds numbers by virtue of both decreased temperature and increased pressure. Preliminary aeroacoustic tests under combined cryogenic and pressurized conditions were conducted by the author[6] at the Pilot-ETW (PETW), a small scale wind tunnel at the ETW site used for research and proof testing. Here, the technical feasibility of performing aeroacoustic measurements within the operated total static pressure and temperature range has been demonstrated on a cylinder as an aeroacoustic source and the results showed significant Reynolds number dependency.

In this study, acoustic array measurements performed at the ETW wind tunnel are described for various Reynolds numbers in the range $1.23 \cdot 10^6$ to $22.18 \cdot 10^6$ (based on the aerodynamic chord length) using an Airbus K3DY half model of scale a 1:13.6 in high-lift configuration.

II. Sensor Calibration for different temperatures and static pressures

For measurements in an environment which is both pressurized and fully cryogenic, the type of sensor used for the microphone array should be able to withstand the harsh conditions and, most importantly, the dependence of its frequency and phase response at the various pressures and temperatures should be known. In this section, the Brüel&Kjær cryogenic-type sensor of type 4944A is introduced and measurements on its amplitude and phase response are presented and evaluated.

At ambient conditions, high precision condenser microphones show a linear frequency response. However, this response does not maintain its frequency response when temperature and static pressure are varied. Until now, this non-linear response has only been investigated separately for each of temperature and static pressure variation. Tests on Brüel&Kjær type 4136 microphones at various static pressures were conducted by Boeing[8] and showed some

rather dramatic frequency response characteristics at high pressures. Those measurements culminated in the design of the special sensor type 4138-W-001, which shows a less dramatic frequency response. Tests on Brüel&Kjær sensor type 4944 at various temperatures were performed by Brüel&Kjær and the ETW GmbH, from which the new cryogenic-type sensor 4944A arose. This microphone type served as a reference for the temperature calibration of the microphones used for the microphone array measurements in the DNW-KKK.[4]

In this work, a calibration measurement was performed using four 1/4-inch Brüel&Kjær cryogenic condenser microphones of type 4944A. The measurements were performed in a cryogenic vessel at the ETW site. Figure 1 shows a photo of the supporting device with the four microphones inside the opened cryogenic vessel. Each microphone was attached to an individual temperature sensor. Additionally, an electrostatic actuator was positioned directly over the microphone membrane. Due to the electrostatic excitation no acoustic insulation was needed inside the vessel.

The advantage of electrostatic excitation is that in the range of our conditions the influence of temperature and static pressure on the produced excitation is negligible. As can be seen in the specifications[9], the produced excitation is dependent of frequency while the dependence on static pressure and temperature is captured by the dielectric constant. The dielectric constant, however changes only slightly[10] from 1.00055 (100 kPa and 290 K) to 1.00556 (450 kPa and 120 K) which leads to a negligible difference in ΔL_p of 0.04 dB.
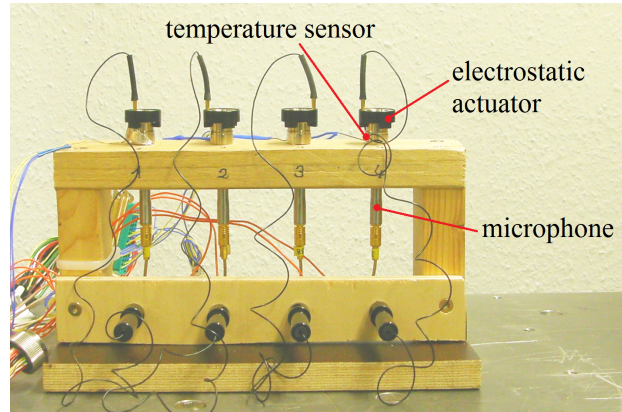

Figure 1. Photo of the supporting device with the four microphones inside the opened cryogenic vessel.

The frequency response was measured under combined cryogenic and pressurized conditions with an excitation signal (sinusoidal sweep) in the range from 500 Hz to 100 kHz. The static pressure was varied in six steps from 110 kPa to 450 kPa and the temperature was altered in 7 steps in the range of 290 K to 120 K. The temperature was measured using Pt100-sensors mounted on the microphone housing.

The average frequency response of the four microphones had only a small standard deviation for all measurement points and frequencies up to 70 kHz. Thus the mean value of the amplitude frequency responses of the four microphones will be used in the following. The figures 2–4 show amplitude responses in decibels normalized to the amplitude response at $T = 290$ K and $p_{stat} = 110$ kPa.

Figure 2 shows the results for $T = 290$ K and various static pressures from 110 kPa to 450 kPa. For increased static pressures, an increased frequency dependency can be observed. The shape of the response curves becomes wavy and a change in response that goes from $+2.9$ dB to -14.7 dB at a static pressure of 450 kPa. Each frequency response curve shows one maximum (in the range of 20 kHz to 22 kHz) and one minimum (in the range of 53 kHz to 60 kHz).

Figure 3 shows the results for $p_{stat} = 110$ kPa and various temperatures from 120 K to 290 K. When temperature is decreased, an increased frequency dependency can also be observed and the shape of the response curves becomes wavy with changes from $+7.5$ dB to -8.7 dB with increased frequency at a temperature of 120 K. The frequency responses for that case show two maxima in the ranges of 22 kHz to 25 kHz and 75 kHz to 90 kHz, and one minimum in the range of 42 kHz to 56 kHz. In contrast to the frequency response shown for changing static pressure, here differences are seen in both the shape of the response curves and the frequency ranges where the maxima and minima occur. The combined influence of non-ambient static pressure and non-ambient temperature on the frequency response can be seen in figure 4. When compared with the previously discussed results, the amplitude response varies more strongly with frequency and the wavy shape of the response curves show maxima and minima that go from -20.1 dB to $+9.0$ dB. As can be clearly seen, the amplitude response to variation of static pressure and temperature is <u>not</u> a linear combination of the amplitude response caused by varying the static pressure or temperature alone. The phase shift between the microphones is of essential importance for the beamforming calculation (see section IV.A). Thus, figure 5 shows the standard deviation of the phase response of the four microphones. In general, the standard deviation of the phase response increases from 0.5 deg at 1 kHz up to approximately 10 deg at 100 kHz. Also, the deviation tends to be higher for increased static pressures. A phase mismatch of 5 deg to 10 deg is within the phase mismatch found for commercially used Array-Microphones[25]. Additionally, the influence on the beamforming result has been estimated by a calculation with a simulated source with due consideration of the measurement setup (microphone positions, focus grid), to be described in section III.A. The distribution of the phase variance for all microphones has been assumed to be rectangular[7]. The influence of a phase variance of 10 deg for all frequencies was shown to be smaller than 0.05 dB for the source amplitude. while the deviation from the source position was less than the focus grid resolution ($d_{xy} = 5$ mm). Thus

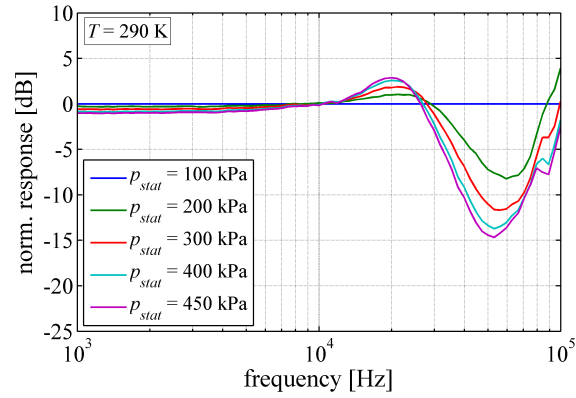the influence of phase variation can be neglected in our setup.

Figure 2. Frequency response of the Brüel&Kjær Type 4944A cryogenic pressure-field 1/4-inch microphones at an ambient temperature of 290 K and various static pressures. The results are normalized to the frequency response at 110 kPa and 290 K.
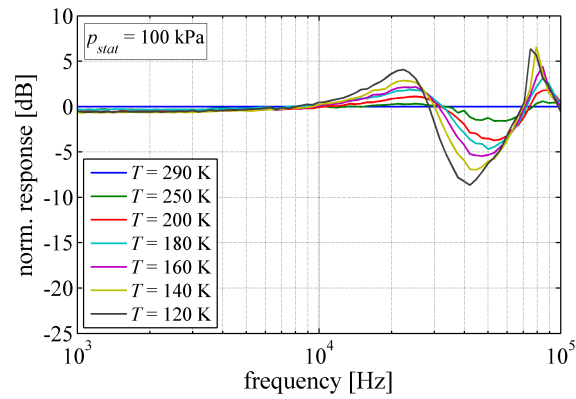

Figure 3. Frequency response of the Brüel&Kjær Type 4944A cryogenic pressure-field 1/4-inch microphones at ambient static pressure (110 kPa) and various temperatures. The results are normalized to the frequency response at 110 kPa and 290 K.
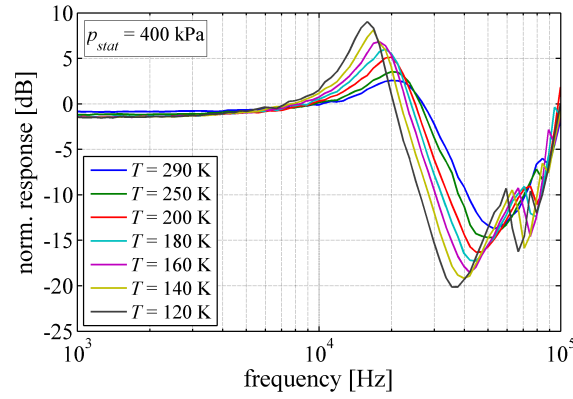
Figure 4. Frequency response of the Brüel&Kjær Type 4944A cryogenic pressure-field 1/4-inch microphones at 400 kPa and various temperatures. The results are normalized to the frequency response at 110 kPa and 290 K.
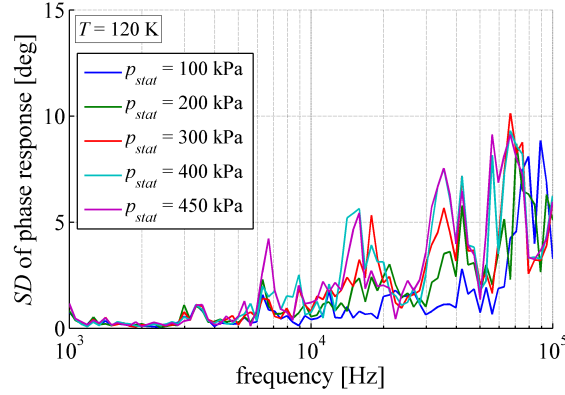

Figure 5. Standard deviation of the phase response of the Brüel&Kjær Type 4944A cryogenic pressure-field 1/4-inch microphones at an ambient temperature of 120 K and various static pressures.

III.   Measurements

A.   Setup

The measurements were performed at the European Transonic Windtunnel ETW located at the ETW Cologne site. The ETW facility is a high Reynolds number transonic wind tunnel of Göttingen-type with a 2.0 m x 2.4 m closed test section. The Mach number range is from 0.15 to 1.35. By injection of liquid nitrogen, the wind tunnel can be operated over a temperature range of 110 to 310 K and the total pressure can be varied between about 115 and 450 kPa. The ETW can thereby provide full-scale (viz. real-flight) Reynolds numbers and independent variation of Reynolds number, Mach number and load. Further details are given in a paper by Quest[11].

Based on the prototype microphone array used for the PETW-test[6], a microphone array suit-

able for cryogenic and pressurized testing consisting of 96 microphones was constructed. For the microphones 1/4-inch cryogenic condenser microphones of type 4944A by Brüel&Kjær were used. The variation in amplitude response caused by varying the static pressure and/or the temperature has already shown in section II. The positioning of microphones is limited to dummy window plates and side wall slot inserts: three dummy window plates and two side wall slot inserts of the test section were used for the installation of the microphones, see figure 6.

The limitation for the microphone positioning leads to strong sidelobes in the beamforming[a] procedure caused by insufficient spatial sampling. Thus, different microphones of the array were used for the evaluation of conventional maps (with no deconvolution applied); however, all microphones were used for the calculation of the deconvoluted CLEAN-SC[13] maps.

Figure 6 shows the 96 microphone positions in the (x, y)-plane. The microphones in the central dummy window were arranged in spiral arms. The two outer dummy windows and the side wall slots lead to an oval arrangement of the microphones. For conventional maps with frequencies greater than 15 kHz the microphones of the central dummy window were used (cyan and red). For frequencies up to 15 kHz, the microphones of the oval circle, the outer circle of the central dummy window and the central microphone were used (blue and red). This entails 44 microphones for covering the low frequency range and 66 microphones for the high frequency range when calculating conventional maps.
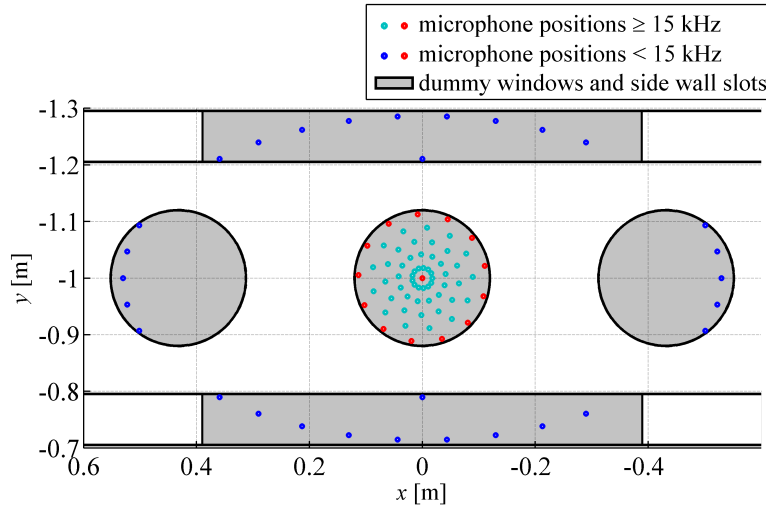

Figure 6. Microphone positions in the (x, y)-plane viewed from outside the test section. For different frequency ranges different microphones are used.

The Airbus K3DY half-model is located in the center of the test section and mounted on

---

[a]see section IV

the top. The model of scale 1:13.6 is installed in landing configuration and has a half-span-width of 1.247 m and a mean aerodynamic chord length of $\delta = 0.308$ m. The model is not equipped with a landing gear. For the whole half-model no tripping device was applied. Table 1 summarizes the half model setup and figure 7 shows a photo of the half-model and the microphone array using the compressed laminated wood inserts in the wind tunnel side wall.

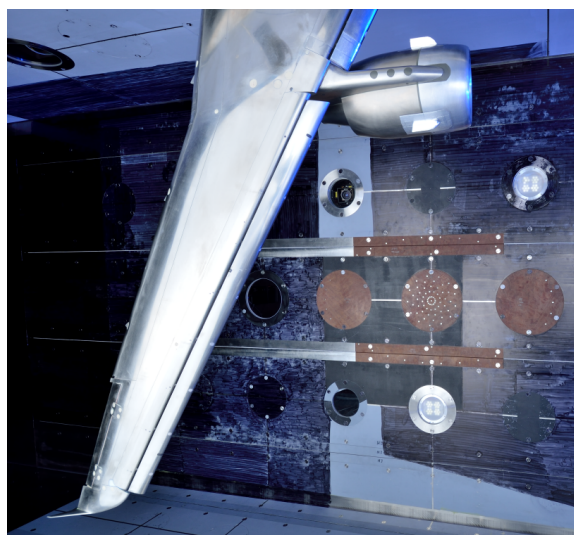| General	
model scale	1:13.6
half span width	1.247 m
aerodynamic chord length	0.308 m
Flap angles	
slat	26 deg
flaps	34 deg
aileron	10 deg

Table 1. Model data.

Figure 7. Photo of the test section with the microphone array mounted into the side wall (wooden inserts) and the K3DY half model in the center. By courtesy of ETW and Airbus.

One important aspect is the increase of load caused by the increased total pressure. Variation of the wind tunnel pressure p_{stat} causes an increased dynamic pressure q, which has an aeroelastic effect on the wing causing wing will deform it. Together with the temperature

dependent Young's modulus E, q/E is a measure for the elastic deformation. This was taken into consideration in the choice of the definition of measurement points, wherewith the effect of the elastic deformation can be separated from the effect of the Reynolds number.

The measurements were performed at three different Reynolds numbers (by way of example values for M = 0.203): $\text{Re}_\delta = 1.43 \cdot 10^6$ as a reference for standard wind tunnels, $5.17 \cdot 10^6$ as an increased Reynolds number and $20.06 \cdot 10^6$ representing the real-flight Reynolds number. The Reynolds number $5.17 \cdot 10^6$ could be achieved in two different ways: by increasing the total pressure at ambient temperature and by decreasing the temperature at ambient pressure. Taking the elastic deformation q/E into account, four data points (DP I to DP IV) were chosen for each Mach number. Table 2 shows the flow parameter for each data point and figure 8 depicts the data points versus the static pressure and the Reynolds number for a Mach number of M = 0.203.

Measurement	Temperature T [K]	Static pressure p_{stat} [kPa]	Reynolds number Re_δ [10^6]	Deformation $q/E[10^{-8}]$	
			M = 0.175	M = 0.203	M = 0.225
DP I	310	110	1.23 (1.16)	1.43 (1.55)	1.58 (1.89)
DP II	125	115	4.47 (1.16)	5.17 (1.55)	5.70 (1.89)
DP III	310	399	4.47 (4.22)	5.17 (5.64)	5.70 (6.88)
DP IV	120	419	17.35 (4.22)	20.06 (5.64)	22.18 (6.88)

Table 2. Flow parameter of the data points DP I to DP VI for Mach numbers of 0.175, 0.203 and 0.225.
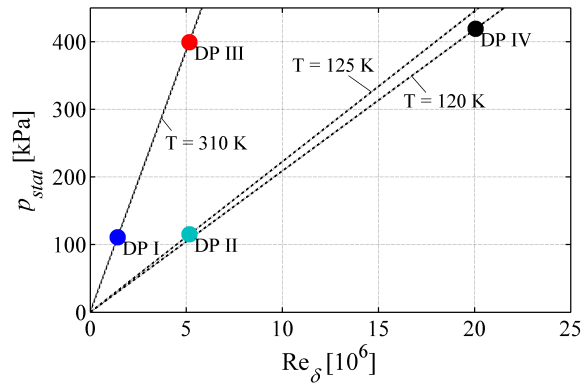

Figure 8. Data points for a Mach number of 0.203 versus the static pressure and the Reynolds number.

This setup of measurement points has the following features:

1. DP I and DP II: same elastic deformation but a different Reynolds number

2. DP III and DP IV: same elastic deformation but a different Reynolds number

3. DP II and DP III: same Reynolds number but different elastic deformation

Thus the effect of the elastic deformation can be separated from the effect of the Reynolds number. In summary, measurements were performed at Mach numbers of 0.175, 0.203 and 0.225 leading to different deformations and Reynolds numbers. The angle-of-attack α at each Mach- and Reynolds number was varied from 3 deg to 9 deg for each data point.

B.   Data Recording

Microphone signals were simultaneously sampled by a data acquisition system located outside the tunnel shell with an A/D conversion of 16 bits and a sampling frequency of 150 kHz. The recording period for each measurement was 30 s. To reduce the influence of the low frequency wind tunnel noise, a second-order high-pass filter with a cut-off frequency of 500 Hz was used. The measured data were corrected with regard to the filter response and the responses for different static pressures and temperatures. The data were processed using an overlap of 50% and a fast-Fourier transform block size of 4096 samples, with a Hanning window, yielding 2197 averages and a narrowband frequency resolution of 36.6 Hz. s

IV.   Data Processing

A.   Beamforming

The array data were processed using the beamforming algorithm in the frequency domain to obtain the reconstructed source auto-powers $\hat{S}_{exp}$ on a grid at scan locations $\mathbf{y_f}$:

$$\hat{S}_{exp}(\mathbf{y}_f, \omega) = \mathbf{e}^{\mathcal{H}} \mathbf{R}_{DR} \mathbf{e}. \tag{1}$$

$\mathbf{R}_{DR}$ denotes the cross-correlation matrix of the microphone signals dependent on frequency ω. The subindex DR denotes that the diagonal term of the cross correlation matrix $\mathbf{R}$ has been set to zero. The phasor $\mathbf{e}$ describes the relevant phase shift based on the point source assumption under homogeneous flow conditions. Additionally, $\mathbf{e}$ incorporates distance scaling in terms of sensor weighting. This was performed using the conventional beamforming approach,[12] which leads to a relative weighting of the sensors to each other, and which is inversely proportional to the source distance from the sensor. $\mathcal{H}$ denotes the conjugate transpose. The array output is calculated on an equidistant discrete grid $(d_{xy} = 5 \text{ mm})$ with 69165 grid points. The grid covers the region of interest in an observation plane of

1.30 m × 1.32 m on the half-model. For each calculation it is rotated by the K3DY model angle-of-attack, whilst also taking into account the dihedral angle. The reconstructed sound power levels are normalized to a reference distance of $r_0 = 1$ m to each grid point. The grid used in the present study can be seen in figure 9.
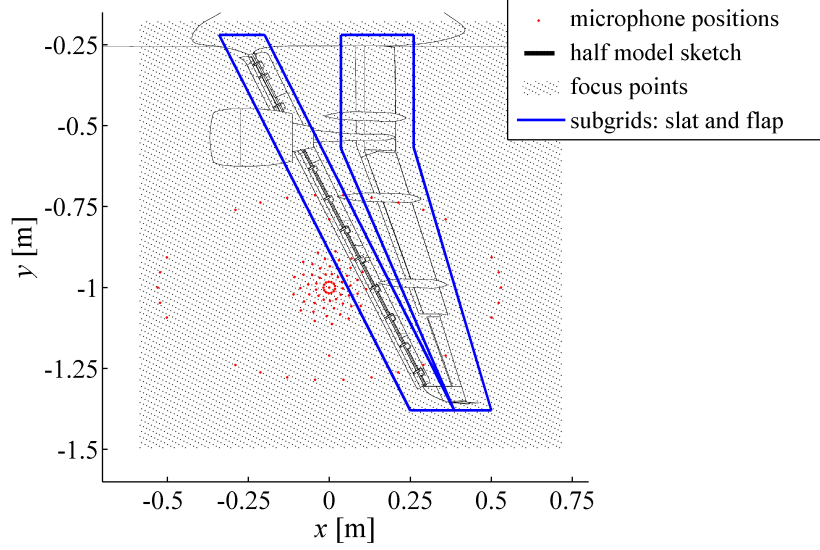

Figure 9. Focus points of the array calculations and the microphone positions in the (x, y)-plane. The location of the half-model is sketched in the background. The subgrid boundaries for the slat and the flap area are sketched with the blue lines.

As illustrated in figure 6, the conventional maps were calculated using different microphones for different frequency ranges. Additionally, source maps were calculated using the CLEAN-SC[13] algorithm. In case of the CLEAN-SC source maps all microphones were used. The sound-pressure-level spectra are obtained by integrating all sources (without the CLEAN-SC residual) found by the CLEAN-SC algorithm over a defined area on the grid.

B.   Condition corrections

In a cryogenic and pressurized test section the acquired data highly depend on the different temperatures and pressures in the test section. For comparability, the influence of those quantities must be considered in terms of a correction.

The evaluation of the measurements leads to a data set of sound pressures depending on the density ρ, the Mach number M, and the speed of sound a. Assuming a perfect gas, its density is described by the ideal gas law:

$$\rho = \frac{p_{stat}}{\mathcal{R}T}. \tag{2}$$

The speed of sound is given by:

$$a(p_{stat}, T) = \sqrt{\frac{\gamma(p_{stat}, T)\mathcal{R}T}{m_{mol}}}.$$ (3)

$\mathcal{R}$ denotes the molar gas constant and m_{mol} the molar mass. Both are constant for pure nitrogen. The slight change of the adiabatic index γ in the examined pressure and temperature range can be obtained from tabulation.[14] Both quantities, ρ and a, depend on the static pressure p_{stat} and the temperature T and affect the radiated sound pressure p'.

Furthermore, a correction is required to take into account the alteration of the radiated sound pressure caused by the different temperatures and pressures. Ideally, this correction would account for the influence of both temperature and pressure on the radiated sound power, so that any remaining variations could be ascribed to changes in Mach- and Reynolds number. This correction will be also dependent on the assumptions made for the nature of the source. Airframe noise sources can be of several types with different mechanisms. Most often, airframe noise sources can be modeled as unsteady forces acting perpendicular to a surface, so called dipole sources.[15–18] Thus in this paper, these kinds of sources are considered to be the main contributing sources from the half model in the test section. As can be derived from the Ffowcs Williams-Hawkings solution of the acoustic analogy with surface sources (see Crighton et al[19], p.334ff; or as has been shown by Curle[20] in a similar manner), the sound generated in terms of the mean-squared density fluctuations ρ' in the far-field for compact[b] dipole sources at low Mach numbers is of order

$$\overline{\rho'^2} \propto \frac{\rho^2 u_\infty^6}{a^6}\frac{D^2}{r^2}.$$ (4)

In equation 4 the parameters dependent on temperature and pressure are now identified in order to obtain a correction for only these parameters. First, the length scale D and the distance r to the source are assumed to be constant. Then the acoustic density fluctuations in terms of the Mach number are of order:

$$\overline{\rho'^2} \propto \rho^2 M^6.$$ (5)

With the acoustic pressure-density relation $p' = \rho'c^2$ derived from the linearized Euler equation, equation 5 can be rewritten as

$$\overline{p'^2} \propto \rho^2 a^4 M^6.$$ (6)

---

[b]compact source: The characteristic length scale D of the source is considerably smaller than the wavelength λ.

For a constant Mach number the decibel correction for dipole sources considering the different temperatures and static pressures in the test section is calculated by:

$$\Delta dB = 20 \log_{10} \left(\frac{\rho a^2}{\rho_0 a_0^2} \right). \tag{7}$$

with $\rho_0 = 1.25$ kg/m^3 and $a_0 = 337$ m/s (c and ρ for pure nitrogen at international standard atmosphere conditions $p_{stat,0} = 101325$ Pa and $T_0 = 288.15$ K). With the help of equation 7 the data acquired at different pressures and temperatures can be normalized. The correction is significant: 12.7 dB for data recorded at $p_{stat} = 420$ kPa and $T = 120$ K.

It should be emphasized that if this correction is applied to the measured data, differences found in the comparison are also dependent on the assumptions made. Thus differences found can be related to an effect of the Reynolds number, the Mach number and deviating source mechanisms, such as, for example, jet noise, cavity noise or noise from non-compact objects.

The $(\rho a^2)^2$-correction from equation 7 is similar to that introduced by Stoker[3] for airframe noise measurements in a pressurized environment. Stoker uses a p_{stat}^2-correction, which he refers to in his paper without, however, showing how it was derived. If the slight change of the adiabatic index γ is neglected (see equation 2 and 3) the $(\rho a^2)^2$-correction is equal to the p_{stat}^2-correction, independent of temperature variations. Deviating from that, Hayes[2] introduced a ρ^2-correction also based on the Ffowcs Williams-Hawkings solution for aerodynamic noise generated in the presence of solid boundaries. This approach is similar to that of the $(\rho a^2)^2$- and p_{stat}^2-correction as long as no temperature variation occurs (see equation 2).

As an additional normalization approach, the results will be compared at the same Strouhal number instead of frequency to account for the different flow velocities, even the Mach numbers are still the same at these different temperatures and pressures (see Ahlefeldt[5]). Here, the Strouhal number will be defined using the mean aerodynamic chord length δ and the free stream velocity u_∞:

$$\text{St}_\delta = \frac{f \cdot \delta}{u_\infty}. \tag{8}$$

As discussed for the application of the condition correction (equation 7), differences found in a comparison can be related to source mechanisms not scaling with the Strouhal number normalized with the free stream velocity and the mean aerodynamic chord length, i.e. cavity noise.

V.   Experimental Results

A.   Source maps

The source maps were computed over the grid region shown in figure 9 using the conventional beamforming method and the CLEAN-SC deconvolution method described previously. The variations in amplitude response for the microphones at different pressures and temperatures as well as the condition correction were applied to the data. In the following, only CLEAN-SC results (without the CLEAN-SC residual) are shown. It should be noted that conventional maps were also computed (but are not shown) for the verification of the sources found by the CLEAN-SC algorithm. For the entire range of frequencies, the widths of the clean beams were set to 5 cm at 3 dB below the peak. As shown in section IV.B, the results are plotted as functions of the Strouhal number St_δ (normalized with the mean aerodynamic cord length δ). With respect to the definition of the Strouhal number (equation 8) and the model scale (see table 1) the chosen Strouhal number range of 20 to 200 corresponds to the full scale frequencies (for standard atmosphere conditions with $p_{stat,0} = 101325$ Pa and $T_0 = 288.15$ K) shown in table 3.

Mach number	Full scale frequency range for $20 \leq St_\delta \leq 200$
0.175	289 Hz $\leq f_{fs} \leq$ 2887 kHz
0.203	335 Hz $\leq f_{fs} \leq$ 3352 kHz
0.225	372 Hz $\leq f_{fs} \leq$ 3722 kHz

Table 3. Full scale frequency ranges at standard conditions for a Strouhal number range of 20 to 200.

Source maps are shown in figure 10 and 11 for a Mach number of M = 0.203 and an angle-of-attack of $\alpha = 3$ deg for different Reynolds numbers (DP I to DP IV). The sound pressure level for the results is normalized to the maximum level of DP I at $St_{\delta,1/3Oct} = 20$. Thus, all source maps from figure 10 and 11 are quantitatively comparable. Each source map is plotted with a dynamic range of 20 dB. To facilitate comparison, the maximum level of this dynamic range in figures 10 and 11 is that appropriate for the maximum level for each Strouhal number band.
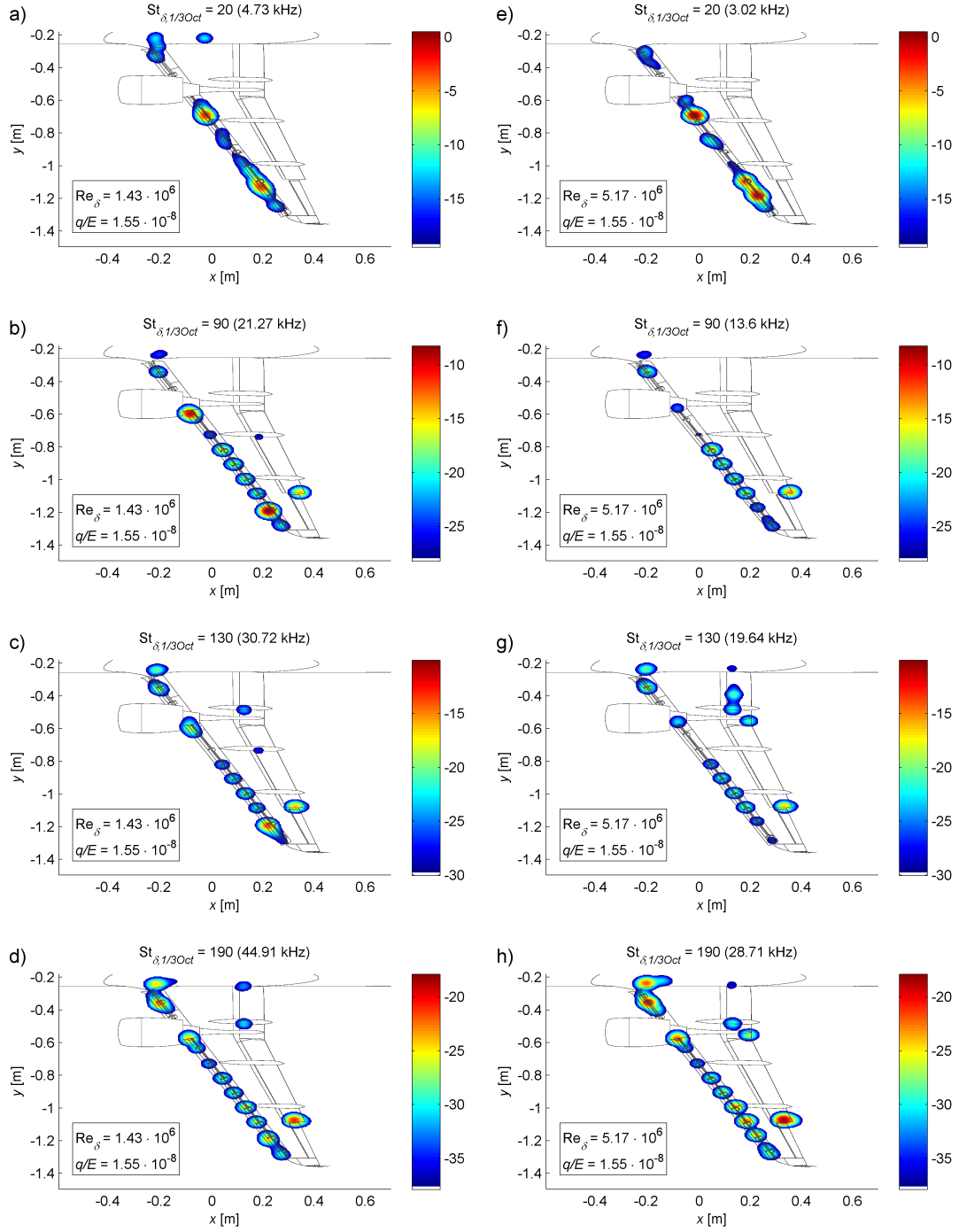
Figure 10. Comparison of the CLEAN-SC source maps (dB) at $M = 0.203$, $\alpha = 3$ deg and $q/E = 1.55 \cdot 10^{-8}$; DP I (a-d): $\mathrm{Re}_\delta = 1.43 \cdot 10^6$; DP II (e-h): $\mathrm{Re}_\delta = 5.17 \cdot 10^6$. Displayed are the 3rd-octave Strouhal number band results normalized to the maximum level of DP I at $\mathrm{St}_{\delta,1/3Oct} = 20$.
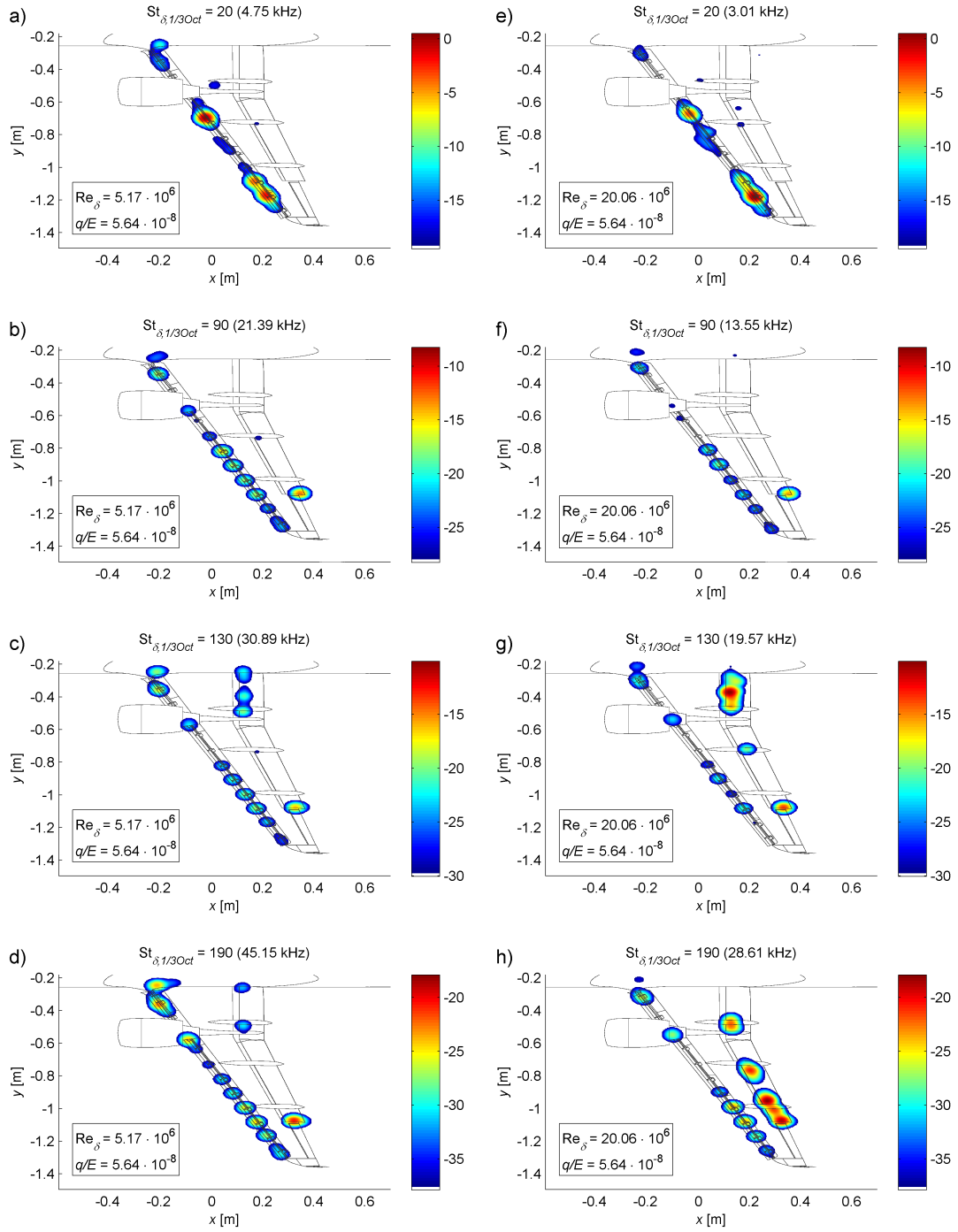
Figure 11. Comparison of the CLEAN-SC source maps (dB) at M = 0.203, $\alpha = 3$ deg and $q/E = 5.64 \cdot 10^{-8}$ DP III (a-d): $Re_\delta = 5.17 \cdot 10^6$; DP IV (e-h): $Re_\delta = 20.06 \cdot 10^6$. Displayed are the 3rd-octave Strouhal number band results normalized to the maximum level of DP I at $St_{\delta,1/3Oct} = 20$.

1. Reynolds number effects

Figure 10 shows a comparison of results at $Re = 1.43 \cdot 10^6$ (left hand column) and $5.17 \cdot 10^6$ (right hand column). The elastic deformation $q/E = 1.55 \cdot 10^{-8}$ is the same for all plots. In general the source maps show dominant sources at the inboard slats, the slat tracks and the flap side edge, with less dominant sources at the flap and the flap track fairings. At a Strouhal number of 20, there are differences on the slat. For one source on the outer slat the level is increased by about 7 dB, and several other sources on the slat show small changes in amplitude up to 3 dB. At Strouhal numbers of 90 and 130, the maps show also a different behavior. The map on the left for the lower Reynolds number shows additional dominant sources on the slat: a source on the slat cove close to the nacelle and a dominant source on an outer slat track. The higher Reynolds number map shows that these sources lose their dominant tonal character. Instead, an additional source of somewhat lower significance appears for a Strouhal number of 130 on the inboard flap side edge. Verified by video surveillance of the test section, this source was attributable to a tape which had become partly detached during the last measurement in the time schedule (DP II). The maps for a Strouhal number of 190 are similar, only that at the higher Reynolds number the overall level is increased by approximately 3 dB.

Figure 11 shows the comparison between $Re = 5.17 \cdot 10^6$ and $Re = 20.06 \cdot 10^6$. The elastic deformation $q/E = 5.64 \cdot 10^{-8}$ is the same for all plots. Up to a Strouhal number of 90 the maps show little variation. Small variations up to 3 dB can be found on the slat tracks and the inner slat. For a Strouhal number of 130, the source map for the real-flight Reynolds number shows considerable differences. Sources with a significantly increased noise level appear on the inner flap and on one flap fairing, with the source level on the flap-side edge being increased by about 3 dB. The sources on the inner flap are the most dominant ones for the real-flight Reynolds number case, where the source levels on the slat are decreased by 3 dB to 5 dB. At a Strouhal number of 190 the source map for the real-flight Reynolds number again shows additional sources. They are the most dominant and can be found on the inner and outer flaps close to the flap fairings.

2. Deformation effects

The effect of the elastic deformation can be observed by comparing DP II and DP III (figure 10 f-h vs. figure 11 a-d). In this comparison the Reynolds number is the same but the elastic deformation is different. For Strouhal numbers up to 90 the comparison shows almost the same map; the sound sources are almost equal in location and source strength. For higher Strouhal numbers the comparison shows in general the same map, but, nevertheless, several differences can still be observed. For the lower q/E an additional source of lower

dominance appears on the inboard flap side edge (which had been attributed to a detached tape) and at a Strouhal number of 190 the overall level of the sources on the slat and the flap is increased by 3 dB to 4 dB.

To conclude, the results obtained at the same Reynolds number but different temperatures (125 K and 310 K), pressures (115 kPa and 399 kPa) and deformation ($1.55 \cdot 10^{-8}$ and $5.64 \cdot 10^{-8}$) lead to almost the same results.

3. Summary

To summarize the observations from the maps, three important statements can be made: First, for low Strouhal numbers up to 100 the Reynolds number and the q/E variations have only a very slight effect on the source maps.

An exception to this are sources on the slat with a strong tonal[c] character, which disappear with a rise of the Reynolds number. In terms of slat cove noise, this is consistent with observations made by for example Dobrzynski[18], that different noise mechanisms occuring at the slat cove – i.e. a) cavity resonances caused by Tollmien-Schlichting boundary layer instabilities, flow separation at the slat hook and b) slat trailing-edge bluntness noise – can be considered a model artifact due to too low Reynolds numbers (a) and manufacturing and handling constraints (b). This observation has also been made by the author in a test with a half model in a cryogenic wind tunnel facility, as mentioned previously.[5]

Secondly, for the real-flight Reynolds number and high Strouhal numbers additional dominant noise sources appear on the flap, possibly related to a thinner boundary layer interacting with the flap gap flow and the flap track fairings and/or the trailing edge of the wing. Based on the observations made, these sources on the flap can be attributed to Reynolds number effects. Thirdly, it was shown that the results obtained at different temperatures, pressures and deformations but the same Reynolds number showed almost the same results.

B. Spectra

1. Entire wing

In the following, sound pressure level spectra are shown. They are obtained by integrating all sources calculated by the CLEAN-SC algorithm (without the CLEAN-SC residual) over the grid region shown in figure 9. The variations in amplitude response for the microphones at different pressures and temperatures as well as the condition correction has been applied to the data.

The spectra for different Reynolds numbers at a Mach number of 0.203 and three different angles-of-attack (3 deg, 7 deg and 9 deg) are compared in figure 12. The results are displayed

---

[c]Those tones have already been investigated previously in experimental[21] and numerical[22] studies

versus the Strouhal number (based on $\delta = 0.308$ m), shown in the range of 20 to 200 for each spectrum.

For each angle-of-attack, the overall shape of the spectra for different Reynolds numbers is similar. From low to high Strouhal numbers, the sound pressure level decreases; this decrease is more pronounced at Strouhal numbers below 100. The results at the three angles-of-attack show differences, as seen in the comparison with the three Reynolds numbers and the two deformation cases. For each angle-of-attack peaks can be found at around $St_\delta \approx 40$ and $St_\delta \approx 55$. For these peaks the amplitude varies with the Reynolds number, while the Strouhal number at which these maxima occur appears to be dependent on the Reynolds number. For angles-of-attack of 3 deg and 9 deg the spectra for the Reynolds number of $1.43 \cdot 10^6$ show several narrow tonal components in the range of $St_\delta = 50$ to $St_\delta = 130$. These tonal components reach levels up to 15 dB above the broadband level. With few exceptions they are not present at increased Reynolds numbers and they disappear completely at the real-flight Reynolds number. As observed in the narrow-band source maps (not shown here), these tones originate from the slat coves and the slat tracks. For an angle-of-attack of 3 deg a broadband increase of about 3 dB to 5 dB can be observed at the real-flight Reynolds number in the range of $St_\delta = 100$ to $St_\delta = 150$. At 7 deg this increase can also be observed for a Reynolds number of $5.17 \cdot 10^6$. Here the broadband increase includes several significant tonal components. In general, at Strouhal numbers above 150 the overall level is increased by 2 to 5 dB for higher Reynolds numbers at angles-of-attack of 3 deg and 7 deg. Remarkably, for the data points DP II and DP IV a broadband increase appears for Strouhal numbers above 140. This increase occurs at all angles-of-attack.

Two major observations can be made from the spectra for the whole wing. First, dominant narrow tonal components at low Reynolds numbers disappear for higher Reynolds numbers, and secondly, several significant broadband increases can be observed for higher Reynolds numbers in the Strouhal number range above 100.
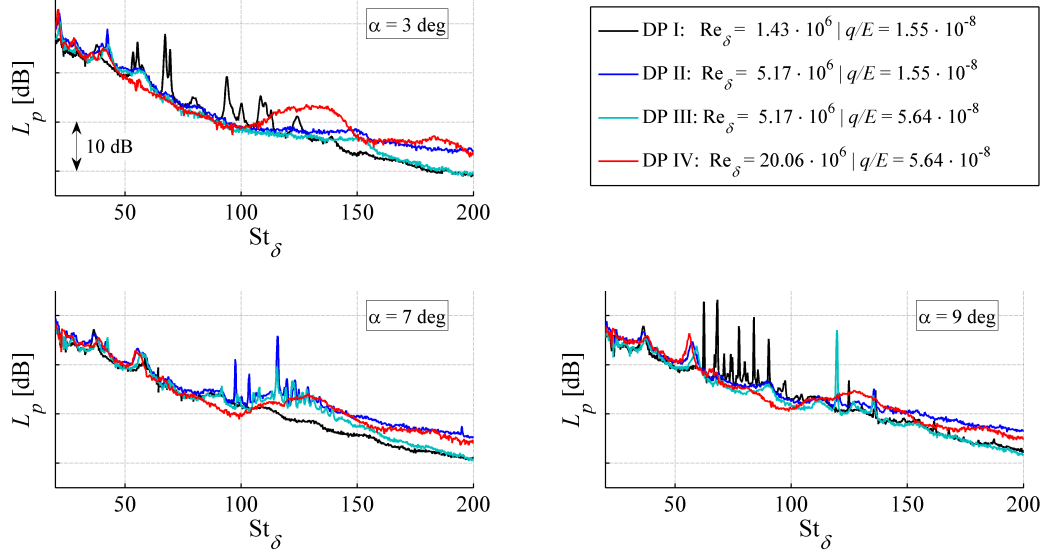
α = 3 deg

DP I: Re$_\delta$ = 1.43 · 10^6 | q/E = 1.55 · 10^{-8}
DP II: Re$_\delta$ = 5.17 · 10^6 | q/E = 1.55 · 10^{-8}
DP III: Re$_\delta$ = 5.17 · 10^6 | q/E = 5.64 · 10^{-8}
DP IV: Re$_\delta$ = 20.06 · 10^6 | q/E = 5.64 · 10^{-8}

L_p [dB]

10 dB

50   100   150   200

St$_\delta$

α = 7 deg

L_p [dB]

50   100   150   200

St$_\delta$

α = 9 deg

L_p [dB]

50   100   150   200

St$_\delta$

Figure 12. Sound pressure level (dB) versus Strouhal number for different Reynolds numbers at a Mach number of 0.203 and different angles-of-attack.

2.   *Background Noise*

For comparison, the sound pressure level spectra for $\alpha = 7$ deg are plotted together with the background noise level in figure 13. The background noise was estimated by using the main diagonal of the cross spectral matrix **R**. Thereby, the background noise contains the boundary layer induced noise as well as acoustic noise radiated from the model and the wind tunnel. By way of example the results from the center microphone (see also figure 6) are shown. The sound pressure level spectra obtained from the cross spectral matrix are corrected using equation 7 and the reference distance also used for the beamformer output $(r_0 = 1$ m$)$. With the condition correction applied it should be noted that in this case the assumptions made for equation 7 are less valid for the sources included in the background noise (boundary layer noise, wind tunnel noise). Figure 13 shows the background noise versus the versus Strouhal number (top) and the frequency (bottom). For comparison the dotted lines show the reconstructed sound power level (dB) for an angle-of-attack of 7 deg.
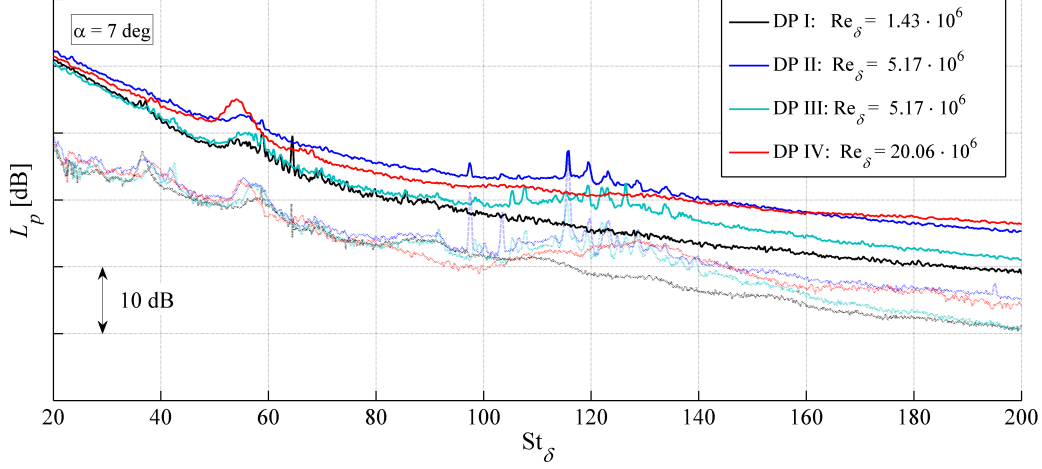
Figure 13. Sound pressure level (dB) of the background noise for different Reynolds numbers at a Mach number of 0.203 versus Strouhal number. For comparison the dotted lines show the reconstructed sound power level (dB) for an angle-of-attack of 7 deg.

The overall shape of the spectra for different Reynolds numbers is similar. For each case spectral components of acoustic sources related to the model are also visible. From low to high Strouhal numbers, the sound pressure level of the background noise decreases. Differences can be found for higher Strouhal numbers. Compared to DP I and DP III the decrease is less pronounced for DP II and DP IV; here the background noise is increased up to 8 dB depend on the Strouhal number. DP III shows a hump around $St_\delta = 120$, due to a dominance of acoustic sources related to the model. In general, the background noise is increased for the cases with the lower temperatures. In comparison with the sound pressure levels reconstructed with the conventional beamforming approach and CLEAN-SC, the background noise was shown to be higher. Nevertheless, as was shown in section V.A, the relevant sources could still be successfully reconstructed.

3.   Subgrids: Slat and Flap

As can be seen in the source maps, sources appear on different areas on the wing. For a simple comparison, the sources on the slat and the flap are separated. Two subgrids were chosen which cover the regions of interest. The sound pressure level for each source region is then obtained by integrating all sources (without the CLEAN-SC residual) calculated by the CLEAN-SC algorithm over the subgrids for the slat and the flap regions shown in figure 9.

The condition correction (equation 7) has been applied to the data.

The spectra for the slat sources are shown on the left side in figure 14. The overall shape of these spectra for different Reynolds numbers is similar. The previously described broadband increase for DP II at Strouhal numbers above 140 is visible for all angles-of-attack. Differences can be observed at different angles-of-attack. At 3 deg two effects of the Reynolds number can be observed: (i) various slat tone peaks, which disappear for higher Reynolds numbers, and (ii) a peak at a Strouhal number of 57 related to the outboard slat close to the nacelle, which disappears only for the flight Reynolds number. At an angle-of-attack of 7 deg the broadband increase around a Strouhal number of 120 with several significant tonal components is of significance. This increase is related to sources on the inboard slat and appears only for a Reynolds number of $5.17 \cdot 10^6$. However, the spectra for $Re_\delta = 1.43 \cdot 10^6$ and $Re_\delta = 20.06 \cdot 10^6$ are very similar. At an angle-of-attack of 9 deg the comparison shows only sporadic differences except for several narrow tonal components at the lowest Reynolds number.

The spectra for the flap sources are shown on the right side in figure 14. Again, the previously described broadband increase for DP II at Strouhal numbers above 140 is visible for all angles-of-attack. The comparison shows a strong Reynolds number dependence for all angles-of-attack. A hump is visible at a Strouhal number of 40. There is a 3 dB decrease in peak height when going from the lowest to the highest (flight-) Reynolds number. For $St_\delta = 50$ to $St_\delta = 100$ the overall level is increased by about 5 dB for the flight Reynolds number. Of major significance is a large broadband increase appearing in the range of $St_\delta = 100$ to $St_\delta = 150$ at the flight Reynolds number and for all angles-of-attack. This hump is related to sources on the inboard flap (see figure 11) and shows a level increase of about 10 dB. A similar peak can be observed in the range of $St_\delta = 125$ to $St_\delta = 165$ at $Re_\delta = 5.17 \cdot 10^6$, also related to sources on the inboard flap. Another significant broadband increase appears around a Strouhal number of 180 for the flight-Reynolds number case. This peak is related to sources on the midboard and inboard flap (see figure 11) and shows a level increase of about 10 dB.
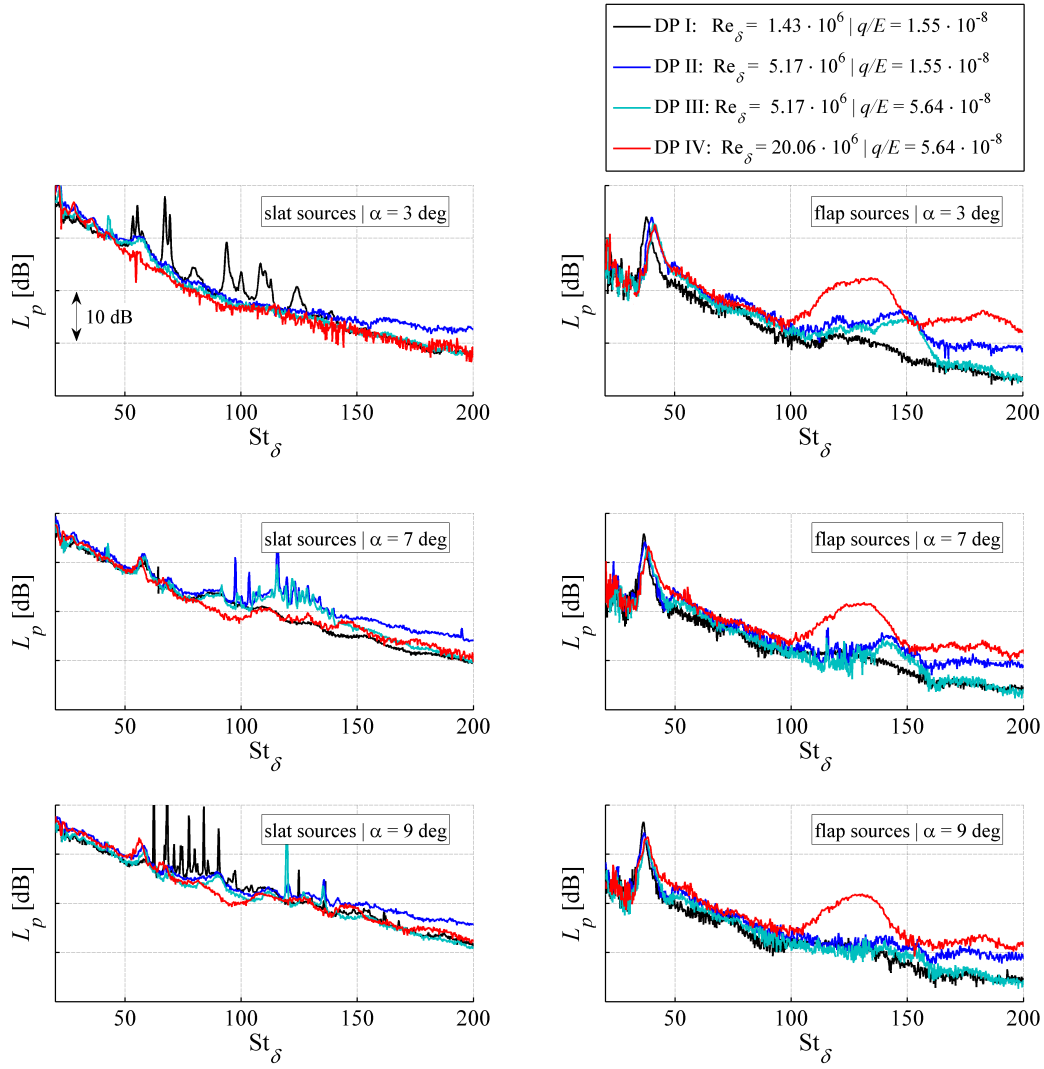
Figure 14. Comparison of slat (left) and flap (right) sources: sound pressure level (dB) versus Strouhal number for different Reynolds numbers and angles-of-attack.

The following observations can be made from the spectra for the slat and the flap regions: Dominant narrow tonal components on the slat at low Reynolds numbers disappear for increased Reynolds numbers. Apart from these narrow tonal components, the spectra for the slat region for different Reynolds numbers are very similar. However, the spectra for the flap region show a strong Reynolds number dependence. This is caused by dominant sources appearing at flight-Reynolds numbers.

4. Discussion

The broadband increase for DP II at Strouhal numbers above 140 was shown to be independent of the different source locations (slat and flap). Thus, it is probably not caused by the change in deformation or changes of other aerodynamic parameters, such as, for example an increased level of turbulence at lower temperatures. Additionally, very large focus point grids were used to look for interfering sources; no relevant sources were found. Consequently, this broadband increase can only be caused by the sensor and/or the method of analysis of the results.

One possible reason could be an uncertainty in the amplitude correction used here for different temperatures and pressures, as presented in section II. For discussion, figure 15 shows the amplitude correction for each of the four data points versus the Strouhal number at a Mach number of 0.203. As can be seen, the correction is significant for each data point and depends strongly on the Strouhal number. Compared to the observed broadband increase in the measured data for Strouhal numbers above 140, the correction of the data point DP II shows a different shape and size. Thus it can be said that here is most probably no systematic error due to the frequency response correction.

Another reason could be an unknown alteration of wind tunnel conditions (i.e. temporary icing), affecting the performance of the sensors or pre-amplifiers. This question will need to be addressed in further tests.
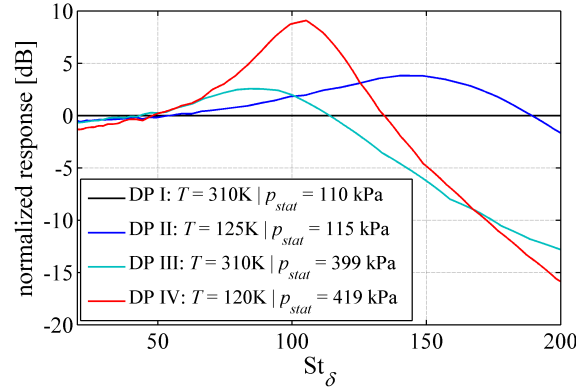

Figure 15. Frequency response of the Bruel&Kjær Type 4944A cryogenic pressure-field 1/4-inch microphones at the different data points DP I to DP IV for a Mach number of 0.203. The results are normalized to the frequency response at 110 kPa and 290 K.

C.   Total sound pressure level

In the following, total sound pressure levels are shown. They are obtained by integrating the sound pressure level obtained by the CLEAN-SC algorithm over a specific grid point area and over an individual Strouhal number range. The condition correction (equation 7) has been applied to the data. Due to the discussed broadband increase at the data point DP II

shown in section B, the results from DP II are not taken into account in this section. Additionally, the Mach number scaling of the sound pressure depending on the angle-of-attack and on certain Reynolds number ranges is shown and discussed. Also the dependence of the acoustic results on the lift, drag and pitching moment was examined. No relationship between these global forces and the radiated acoustic pressures could be found. As, for example, shown by Kröber[24], the information obtained from global forces is of little relevance for interpretation of these aeroacoustic studies, since only the local forces in the wing section are relevant for the source. These local values, however, were not measured in this work.

1.   Entire wing

Figure 16 depicts the total sound pressure level integrated over the whole focus point grid shown in figure 9 and integrated over a Strouhal number range from 20 to 200. Each subplot represents the result for one angle-of-attack versus the Reynolds number, where the different line styles refer to the different Mach numbers. In general, the sound pressure level increases slightly with the Reynolds number by about 1 dB. This increase is related to the previously mentioned broadband increase for increased Reynolds numbers on the inner and outer flap. Deviations from this behavior occur at all Mach numbers at the lowest Reynolds numbers for $\alpha = 3$ deg, M $= 0.175$ and $\alpha = 9$ deg. This is related to the previously mentioned dominant sources on the slat with a strong tonal character, which disappear with a rise of the Reynolds number.

In analogy to figure 12, one would expect an increased total sound pressure level for the low Reynolds numbers caused by the tonal components of the dominant sources on the slat, especially for $\alpha = 3$ deg and $\alpha = 9$ deg. For $\alpha = 3$ deg the tonal components from the slat at low Reynolds numbers are compensated by several spectral components for the higher Reyonolds numbers. These are peaks at very low Strouhal numbers $St_\delta \approx 25$ and the broadband increase above $St_\delta = 100$. For $\alpha = 9$ deg the tonal components are mainly compensated by the peak at $St_\delta \approx 55$. Thus the integration over the whole Strouhal number range from 20 to 200 gives only a general overview and does not accounts for all major effects.
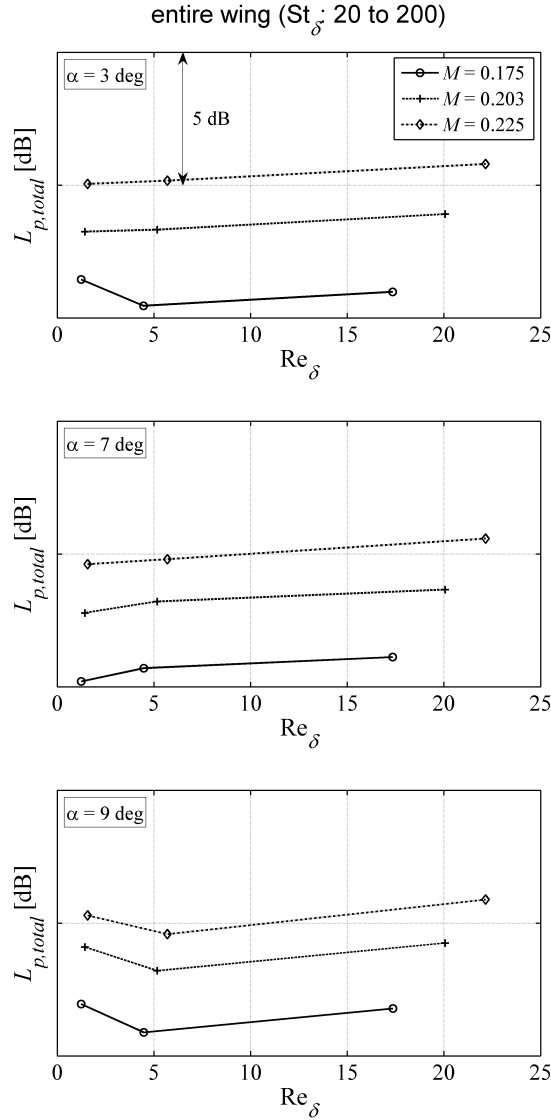
Figure 16. Total sound pressure level (dB) versus Reynolds number for different Mach numbers at different angles-of-attack. Displayed are the results from DP I, DP III and DP IV. Regarding DP II see section V.B.4.

Figure 17 depicts the Mach number scaling exponent of the total sound pressure. It was derived from the results by a least squares fit for the Reynolds number range of the data points DP I to DP IV. It has to be noted that here there would be an error in the interpretation of the obtained results if the change of the Reynolds number within the respective Reynolds number range had a significant influence on the total sound power. Therefore the error-bar shown in the figure illustrates the standard deviation within the respective Reynolds number range. In general, the scaling exponent is in the range of 3 to 4.5, dependent on the Reynolds number range and angle-of-attack. Low Reynolds numbers (DP I) show the smallest Mach

number scaling exponents for angles-of-attack of 3 deg and 9 deg. In comparison to figure 14 this is probably related to the domination of the slat tones, whose scaling is less dependent on the Mach number than on the Reynolds number. For the mid (DP III) and real-flight (DP IV) Reynolds numbers the scaling exponent decreases almost linearly from about 4.3 to about 3.6. From figure 14 it can be seen that the dominant sources are broadband, tonal slat sources and broadband peak sources on the inner and outer flap. The decrease of the exponent with angle-of-attack is most likely related to the also decreasing domination of the broadband peak source on the inner and outer flap. The source on the inner flap will be discussed in the next subsection.

As opposed to the Mach number scaling for the entire wing found in these measurements (M^3 and $M^{4.5}$), one can find in the literature[17, 23] that the sound pressure level of high-lift configurations scales usually between M^5 and M^6. It was shown in the measurements in this paper that this is probably related to sources which are less dependent on the Mach number than on the Reynolds number.
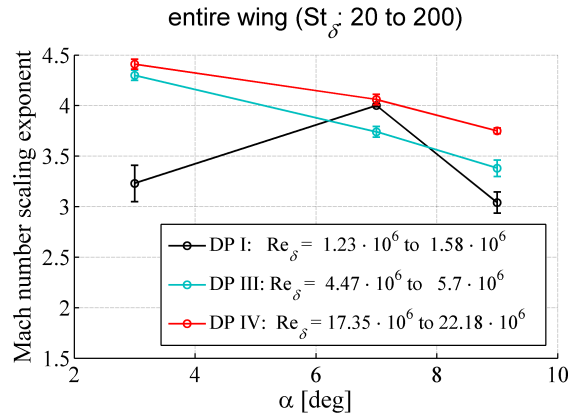

Figure 17. Mach number scaling exponent versus angle-of-attack for different Reynolds number ranges. Displayed are the results from DP I, DP III and DP IV. Regarding DP II see section V.B.4.

2. Inner flaps

Figure 18 shows the total sound pressure level integrated over the inner flap area (subgrid: inner flap with $y < -0.57$ m) shown in figure 9 and integrated over a Strouhal number range from 100 to 165. Each subplot represents the result for one angle-of-attack versus the Reynolds number, where the different lines refer to the different Mach numbers. Two important observations can be made. First, the sound pressure level increases significantly with the Reynolds number by about 20 dB. This increase is more pronounced for the lower Reynolds number range. Second, the influence of the Mach number appears to be less significant than the scaling with the Reynolds number.

As also shown for the entire wing, figure 19 depicts the Mach number scaling exponent of the total sound pressure for the Reynolds number range of the data points DP III and DP IV. Again, the scaling exponent was derived from the results by a least squares fit for the Reynolds number. Because the source is not present at low Reynolds numbers the results of DP I are not shown. In general, the exponent is in the range of 3 to 5.5. The highest exponents (5 to 5.5) are found for the real-flight Reynolds number range. Here the angle-of-attack has only a small influence on the Mach number scaling. For the mid Reynolds number range (DP III), the exponent decreases markedly with increasing angle-of-attack. The results also demonstrate an increased standard deviation. In comparison to figure 14 this is probably related to a less significant source at higher angles-of-attack. Thus the scaling exponent of this source cannot be determined suffiently accurately. In general, the Mach number scaling in the range M^5 to $M^{5.5}$ indicates a dipole-like source mechanism for the source on the inner flap.
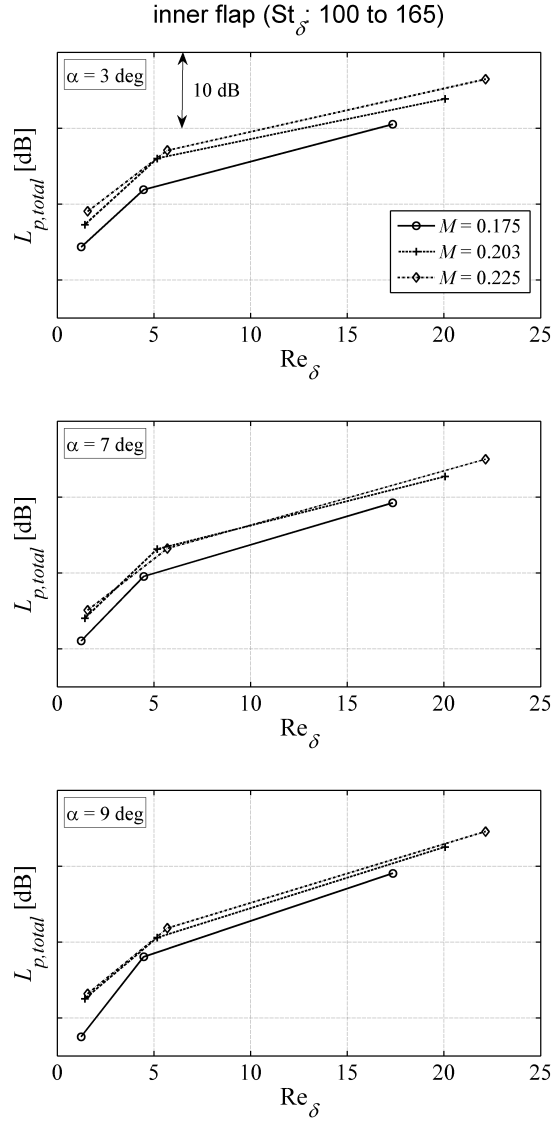
Figure 18. Total sound pressure level (dB) versus Reynolds number for different Mach numbers at different angles-of-attack. Displayed are the results from DP I, DP III and DP IV. Regarding DP II see section V.B.4.
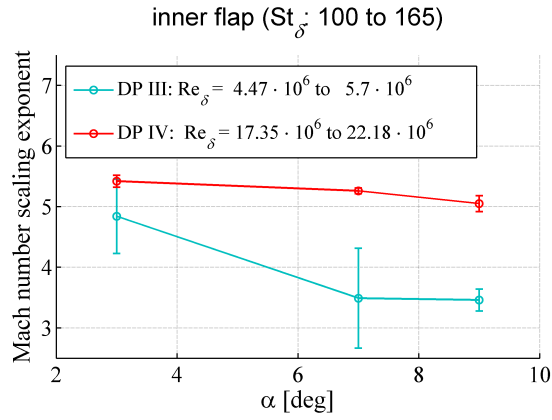
Figure 19. Mach number scaling exponent versus angle-of-attack for different Reynolds number ranges. Displayed are the results from DP III and DP IV.

VI.   Summary and Outlook

The DLR performed microphone array measurements at combined pressurized and cryogenic conditions in the European Transonic Windtunnel (ETW). In this demonstration experiment, the sound radiation from an Airbus K3DY half-model in a high-lift configuration was successfully measured from Reynolds numbers of $1.23 \cdot 10^6$ up to real-flight Reynolds numbers of $22.18 \cdot 10^6$. To this end, a microphone array consisting of 96 microphones has been developed, constructed and installed in the wind tunnel. The important outcomes of this study are:

1. To our knowledge, this is the first time that airframe noise data of a small-scale model have been acquired at real-flight Reynolds numbers.

2. In general, there are several sources with a significant Reynolds number dependency; for example, sources on the inboard slat only appear at mid-level Reynolds numbers, dominant sources on the flap at real-flight Reynolds number and various peaks in the spectra with combined Strouhal- and Reynolds number dependencies.

3. A condition correction has been presented, derived from the ideal gas law and the far-field of compact dipole sources. With this correction the data acquired at different pressures and temperatures can be normalized. With this applied condition correction the spectra showed very similar levels. The assumptions concerning the sound radiation have thus been confirmed for this measurement and have been shown to be helpful in identifying sources with significant Reynolds number dependencies.

4. The effect of the elastic deformation has been obtained by comparing measurements at different temperatures and pressures but the same Reynolds number. The comparison

shows almost the same results; here the effect of the elastic deformation has a very little impact.

5. For Strouhal numbers up to 100 the Reynolds number has a small effect on the overall radiated airframe noise. Exceptions to this are sources on the slat with a strong tonal character, which disappear with a rise of the Reynolds number, and various peaks with combined Strouhal- and Reynolds number dependencies.

6. For Strouhal numbers above 100 very significant broadband peak increases can be observed for real-flight Reynolds numbers. They are caused by various dominant sources appearing on the flap at real-flight Reynolds numbers, possibly related to a thinner boundary layer interacting with the flap gap flow and the flap track fairings and/or the trailing edge of the wing.

The ability of measuring airframe noise at real-flight Reynolds numbers gives now the possibility of separating the effect of the Reynolds number from the effects of model-fidelity and Mach number on aeroacoustic behavior. In order to demonstrate the suitability of aeroacoustic small-scale model measurements two further steps are necessary. First, the results from these tests should be compared with wind tunnel tests of full scale model parts at the same aerodynamic conditions, and second, ultimately, with flyover tests. This encompasses several issues: for example, the attainment of comparable conditions and the related determination of the most important factors (e.g. pressure distribution, flyover/wind tunnel corrections, model-fidelity and deformation).

VII.   Acknowledgements

References

[1] R. W. Stoker, Y. P. Guo, G. Street and N. Burnside, "Airframe Noise Source Location of a 777 Aircraft in Flight and Comparisons with Past Model Scale Tests," *AIAA-2003-3232, 9th AIAA/CEAS Aeroacoustics Conference*, 2003.

[2] J. A. Hayes, W. C. Horne,S. M. Jaeger, and P. T. Soderman, "Measurement of Reynolds number effect on airframe noise in the 12-foot pressure wind tunnel," *AIAA-1999-1959, 5th AIAA/CEAS Aeroacoustics Conference and Exhibit*, (1999).

[3] R. W. Stoker, R. Gutierrez, J. V. Larssen, J. R. Underbrink, G. M. Gatlin and C. Spells, "High Reynolds Number Aeroacoustic Testing in NASAs National Transonic Facility (NTF)," *AIAA-2008-838, 46th AIAA/CEAS Aerospace Science Meeting and Exhibit*, (2008).

[4] T. Ahlefeldt and L. Koop, "Microphone Array Measurements in a Cryogenic Wind Tunnel," *AIAA-Journal*, Vol. 48, No. 7 (2010), pp. 1470–1479.

[5] T. Ahlefeldt, "Aeroacoustic Measurements of a Scaled Half-Model at High Reynolds Numbers," *AIAA-Journal*, Vol. 51, No. 12 (2013), pp. 2783–2791

[6] T. Ahlefeldt and J. Quest, "High-Reynolds Number Aeroacoustic Testing Under Pressurised Cryogenic Conditions in PETW," *AIAA-2012-0107, 50th AIAA Aerospace Sciences Meeting including the New Horizons Forum and Aerospace Exposition*, (2012).

[7] P. Castellini and M. Martarelli, "Acoustic beamforming: Analysis of uncertainty and metrological performances," *Mechanical Systems and Signal Processing* , Vol. 22, pp. 672–692, (2008).

[8] T. Mueller (editor), "Aeroacoustic Measurements", *Experimental Fluid Mechanics*, Springer-Verlag Berlin Heidelberg New York, 2002, p. 163.

[9] "Microphone Handbook. Vol.1: Theory", *Brüel&Kjær*, BE 1447 11, pp. 2-55ff, (1996)

[10] B. A. Younglove, "Thermophysical properties of fluids. I. argon, ethylene, parahydrogen, nitrogen, nitrogene trifluride and oxygen", *Journal of Physical and Chemical Reference Data*, Vol. 11, (1982)

[11] J. Quest, "ETW - High quality test performance in cryogenic environment," *AIAA-2000-2260, 21st Aerodynamic Measurement Technology and Ground Testing Conference*, (2000).

[12] P. Sitsma, "Experimental techniques for identification and characterisation of noise sources," *Advances in Aeroacoustics and Applications*, VKI Lecture Series, (2005).

[13] P. Sitsma, "CLEAN based on spatial source coherence," *International Journal of Aeroacoustics*, Vol. 6, (2007), pp. 357–374.

[14] J. Hilsenrath, C. W. Beckett, W. S. Benedict, L. Fano, H. J.Hodge, J. F. Masi, R. L. Nuttall, Y. S. Touloukian and H. W.Woolley, *Tables of Thermal Properties of Gases*, National Bureau of Standards Circular 564, Washington D.C., (1955).

[15] D. G. Crighton, "Airframe Noise," *In: NASA. Langley Research Center, Aeroacoustics of Flight Vehicles: Theory and Practice. Volume 1: Noise Sources pp. 391–447*, (1991).

[16] P. T. Sodermann, F. Kafyeke, N. J. Burnside, R. Chandrasekharan, S. M. Jaeger and J. Boudreau, "Airframe noise study of a CRJ-700 aircraft model in the NASA Ames 7- by 10-Foot Wind Tunnnel No. 1," *AIAA-2002-2406, 8th AIAA/CEAS Aeroacoustics Conference and Exhibit*, (2002).

[17] Y. P. Guo and M.C. Joshi, "Noise characteristics of Aircraft High Lift Systems," *AIAA-Journal*, Vol. 41 (2003), pp. 1247–1256.

[18] W. Dobrzynski, "Almost 40 Years of Airframe Noise Research: What Did We Achieve?," *Journal of Aircraft*, Vol. 47, No. 2, (2010), pp. 353–367.

[19]D. G. Crighton, A. P. Dowling, J. E. Ffwocs Williams, M. Heckl, F. G.Lipperton, *Modern Methods in Analytical Acoustics: Lecture Notes*, Springer-Verlag Berlin Heidelberg New York, (1992).

[20]N. Curle, "The Influence of Solid Boundaries upon Aerodynamic Sound," *Proceedings of the Royal Society of London. Series A, Mathematical and Physical Sciences*, Vol. 231 (1955), pp. 505–514.

[21]Dobrzynski, W. and Pott-Polenske, M., "Noise Source Studies for Farfield Noise Prediction," *AIAA-2001-2158, 7th AIAA/CEAS Aeroacoustics Conference*, 2001.

[22]Khorrami, M. R., "Understanding Slat Noise Sources," *Colloquium EUROMECH 449*, 2003.

[23]W. Dobrzynski, B. Gehlhar and H. Buchholz "Model and full scale high-lift wing wind tunnel experiments dedicated to airframe noise redution," *Aerospace and Technology*, Vol. 5, No. 1, (2001), pp. 27-33.

[24]Kröber, S. and Koop, L., "Comparison of Microphone Array Measurements of an Airfoil with High-Lift Devices in Open and Closed Wind Tunnels," *AIAA-2001-2158, 7th AIAA/CEAS Aeroacoustics Conference*, 2001.

[25]Brüel&Kjær, "Product Data, 20 kHz Array Microphone - Type 4951"